Energy Storage Materials 71 (2024) 103618

Contents lists available at ScienceDirect

Energy Storage Materials

journal homepage: www.elsevier.com/locate/ensm

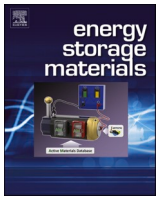

$KTaCl_6$: High-voltage stable potassium-ion conducting chloride solid electrolyte

Changhoon Kim [a], Juhyoun Park [a], Hiram Kwak [a], Jae-Seung Kim [b], Seunggoo Jun [a], Dong-Hwa Seo [b], Yoon Seok Jung [*,a]

[a] Department of Chemical and Biomolecular Engineering, Yonsei University, Seoul 03722, Republic of Korea
[b] Department of Materials Science and Engineering, Korea Advanced Institute of Science and Technology (KAIST), Daejeon 34241, Republic of Korea

ARTICLE INFO

Keywords:
Potassium-ion batteries
Halide solid electrolytes
Mechanochemical syntheses
Three-electrode cyclic voltammetry
Ionic conductivities

ABSTRACT

The exceptional electrochemical oxidative stabilities of halide solid electrolytes (SEs) have led to extensive research on Li and Na all-solid-state batteries. In this study, we report a new K^+ SE, cubic $KTaCl_6$, with a remarkable K^+ conductivity of 1.0×10^{-5} S cm^{-1}, synthesized via a mechanochemical method. This value represents a 1000-fold enhancement over that of samples prepared through heat treatment, which is remarkable among halide K^+ SEs reported to date. Through structural characterization via X-ray diffraction, Rietveld analysis, and bond valence energy landscape calculations, we reveal three-dimensional K^+ migration pathways facilitated by face-sharing KCl_{12}^{11-} cuboctahedra. This configuration is in contrast to that of the monoclinic $KTaCl_6$ produced through annealing, which features discontinuous K^+ migration pathways. These pathways are formed by the edge- or corner-sharing of KCl_{12}^{11-} anti-cuboctahedra, resulting in a significantly reduced K^+ conductivity. Cyclic voltammetry measurements employing three-electrode cells indicate high electrochemical stability up to ≈3.7 V (vs. K/K^+).

1. Introduction

Potassium chemistry in rechargeable batteries may be promising for achieving cost-effectiveness with high energy density owing to the abundance of potassium and its low potential (0.104 V vs. Li/Li^+) [1,2], which is appealing for large-scale energy storage systems [3,4]. Furthermore, following the development pathways of Li and Na technologies [5-9], the advent of all-solid-state K or K-ion batteries with inorganic K^+ solid electrolytes (SEs) has the potential to enhance safety and energy density compared with their counterparts employing liquid electrolytes.

To date, the range of identified inorganic K^+ SEs remains narrow, encompassing oxides, sulfides, and halides [10-13]. Oxide K^+ SEs, specifically $K_{1.6}Mg_{0.6}Al_{10.4}O_{17}$ and $K_2Fe_4O_7$, demonstrated high ionic conductivities, exceeding 10^{-4} S cm^{-1} at room temperature [10,11]. However, these materials require a deleterious high-temperature sintering process (typically above 700 °C) to mitigate the grain boundary resistance. Recently, sulfide and selenide K^+ SEs were identified, exhibiting high ionic conductivities through an aliovalent substitution strategy that creates K vacancies ($K_{2.92}Sb_{0.92}W_{0.08}S_4$: 1.4×10^{-4} S cm^{-1} at 40 °C [12] and $K_{2.2}Ba_{0.4}SbSe_4$: 1.0×10^{-4} S cm^{-1} at 40 °C) [13]. However, the electrochemical oxidative stability of sulfide K^+ SEs constrains their potential for high-voltage applications exceeding ≈3 V (vs. K/K^+) [12]. Moreover, despite being much less prevalent than their oxide counterparts, sulfide and selenide K^+ SEs suffer from significant challenges owing to their high grain boundary resistances. These resistances are considerably higher than those of Li^+ or Na^+ sulfide SEs. This can be explained by their increased ionic character, which is a consequence of the larger ionic size of K^+, following Fajan's rule [14-18].

The origin of recent intensive developments in Li^+ and Na^+ halide SEs can be traced back to the reinvestigation of mechanically prepared Li_3YCl_6 in 2018 [19]. This material demonstrated a moderate conductivity of 0.51 mS cm^{-1} with excellent electrochemical compatibility with unprotected $LiCoO_2$ [20,21]. The pivotal discovery spurred subsequent investigations into Li^+ halide SEs [22], leading to the identification of novel compounds, including Li_3InCl_6 [23], Li_3ScCl_6 [24], and Li_2ZrCl_6 [25]. Furthermore, research efforts have been extended to substituted variants, such as $Li_{3-x}M_{1-x}Zr_xCl_6$ (M = Y, Er) [26], $Li_{3-3x}M_{1+x}Cl_6$ (M = Tb, Dy, Ho, Y, Er, Tm) [27], and $Li_{2+x}Zr_{1-x}M_xCl_6$ (M = Fe, V, Cr) [21].

* Corresponding author.
E-mail address: yoonsjung@yonsei.ac.kr (Y.S. Jung).

https://doi.org/10.1016/j.ensm.2024.103618
Received 12 April 2024; Received in revised form 9 June 2024; Accepted 2 July 2024
Available online 3 July 2024

Specifically, structural alterations and adjustments to Li^+ concentration through compositional tuning are two pivotal factors that influence Li^+ conductivity. Similar exploratory pathways have been pursued for Na^+ halide SEs, although the variety and conductivity of the developed compositions are much lower, with fewer examples, such as Na_2ZrCl_6 [28], $Na_{3-x}Er_{1-x}Zr_xCl_6$ [29], $Na_{3-x}Y_{1-x}Zr_xCl_6$ [30], and ZrO_2–$2Na_2ZrCl_5F$ [31]. In the evolving landscape of halide SEs, the application of extensive mechanochemical preparation protocols has been instrumental in achieving favorable structural frameworks and microstructures [32,33]. This method has led to ionic conductivities that are higher by more than an order of magnitude than those of samples prepared via traditional heat treatment methods. Notable examples include Li_2ZrCl_6 (mechanically prepared trigonal structure: 4.0×10^{-4} S cm^{-1} vs. annealing prepared monoclinic structure: 5.7×10^{-6} S cm^{-1}) [21], Na_2ZrCl_6 [28], and $NaAlCl_4$ [34].

The recent emergence of Ta-based halide SEs marks a significant milestone, as they have demonstrated exceptionally high ionic conductivities of up to 10 mS cm^{-1}. $LiTaCl_6$ and its variants, subjected to rigorous mechanical milling for an extended time over 200 h, exhibited remarkable ionic conductivities of 11 mS cm^{-1}, which was attributed to their amorphous structure [32]. Concurrently, $LiMOCl_4$ (M = Nb and Ta), featuring a structure with corner-sharing oxygen, achieved a maximum ionic conductivity of 12.4 mS cm^{-1} at 25 °C [33]. Shifting to Na analogs, novel compounds have been identified, such as $NaTaCl_6$ (4.0 mS cm^{-1} and 6.2×10^{-5} S cm^{-1}) [35,36], $0.5Na_2O_2$-$TaCl_5$ (4.6 mS cm^{-1} at 25 °C) [37], $Na_{0.86}SmTa_{0.43}Cl_6$ (1.2 mS cm^{-1} at 25 °C), and $NaLa_{0.83}Ta_{0.5}Cl_6$ (1.4 mS cm^{-1} at 25 °C) [38].

However, the exploration of K^+ halide SEs has been markedly limited, with only a few compounds identified to date. The first, $K_{2.3}Zr_{0.7}Y_{0.3}Cl_6$, demonstrated a K^+ conductivity of 9.2×10^{-7} S cm^{-1} at 25 °C [39]. The observed increase in ionic conductivity owing to Y doping was attributed to facilitated K^+ migration into vacant octahedral sites in the expanded lattices. The other identified compounds, featuring a UCl_3 structure and consisting of $1.5KCl$-$(LaCl_3{\cdot}CeCl_3{\cdot}ZrCl_4{\cdot}HfCl_4{\cdot}TaCl_5)_{0.2}$ and KCl-$LaCl_3$–$0.5TaCl_5$ showed ionic conductivities of 1.3×10^{-6} and 1.2×10^{-4} S cm^{-1}, respectively [40,41].

In this study, we present a new K^+ halide SE, $KTaCl_6$, prepared via mechanochemical methods, demonstrating an impressive ionic conductivity of 1.0×10^{-5} S cm^{-1} at 30 °C. This value has been achieved without the need for hot-sintering or pressing. Structural analysis using X-ray diffraction (XRD) Rietveld refinement and bond valence energy landscape (BVEL) calculations revealed that ball-milled $KTaCl_6$ (BM-$KTaCl_6$) adopts a cubic structure. This structure facilitates the formation of three-dimensional (3D) isotropic K^+ migration channels through face-

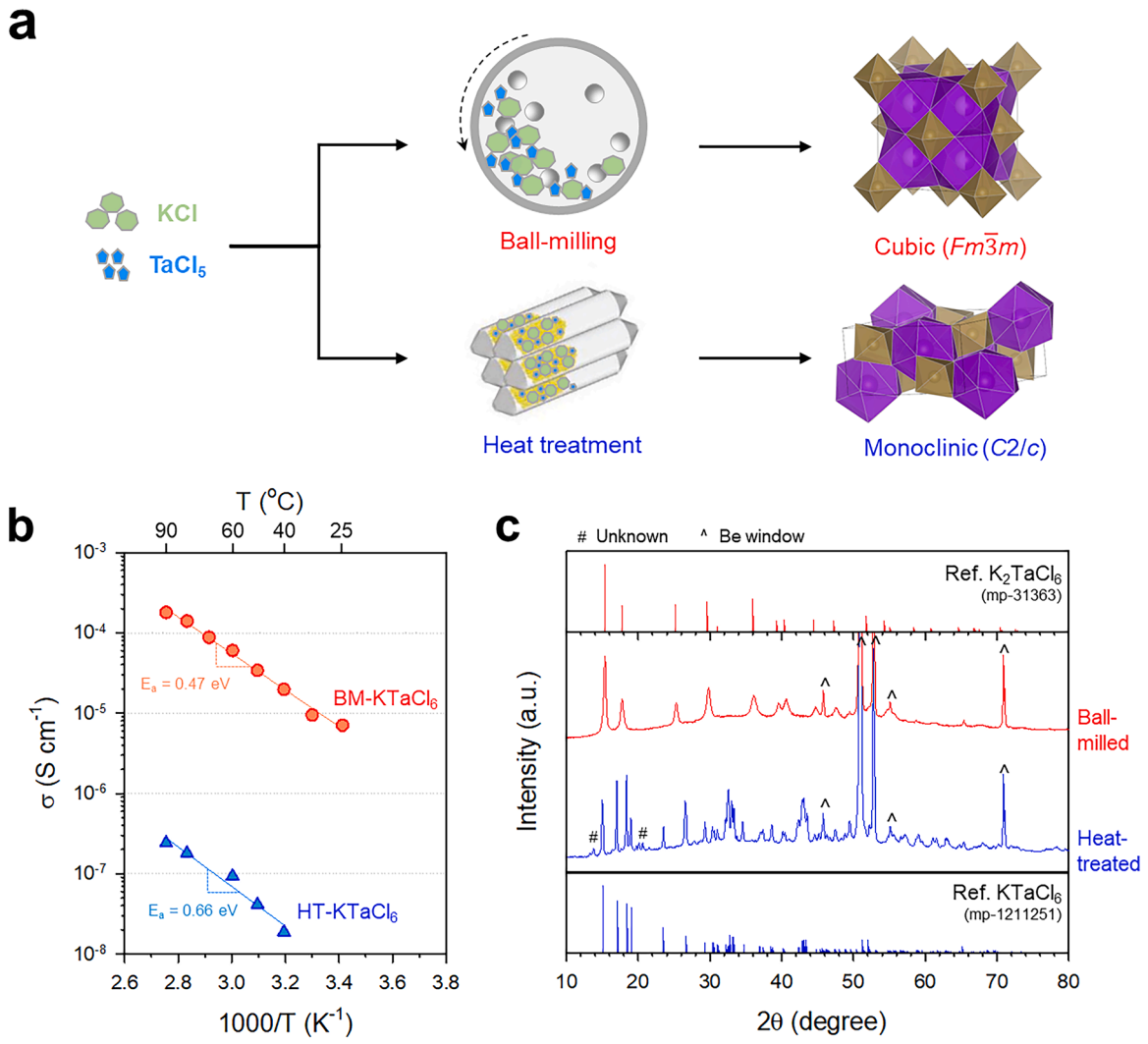

Fig. 1. Preparation and characterization of $KTaCl_6$ prepared via a mechanochemical method vs. heat treatment. a) Schematic illustrating the phase evolutions in $KTaCl_6$ prepared via ball-milling (BM) and heat treatment (HT). The purple and dark yellow polyhedra represent $TaCl_6^-$ and (b) KCl_{12}^{11-}, respectively. b) Arrhenius plots of K^+ conductivities and c) XRD patterns of $KTaCl_6$ prepared using BM and HT. Bragg peaks for K_2TaCl_6 and $KTaCl_6$ are plotted as references at the top and bottom, respectively.

sharing KCl_{12}^{11-} cuboctahedra. Conversely, $KTaCl_6$ prepared via heat treatment at 500 °C (HT-$KTaCl_6$) has a monoclinic structure, which lacks connectivity in the K^+ migration pathways. This structural limitation explains the substantially lower K^+ conductivity of 1.2×10^{-8} S cm^{-1}. Additionally, meticulous measurements employing three-electrode cells facilitated the analysis of the electrochemical stability of $KTaCl_6$, revealing a stability window between approximately 2.7 V and 3.7 V (vs. K/K^+). These findings are compared with the results of density functional theory (DFT) calculations.

2. Results and discussions

Two different $KTaCl_6$ samples, BM-$KTaCl_6$ and HT-$KTaCl_6$, were prepared via ball-milling and heat treatment at 500 °C, respectively, from an equimolar mixture of KCl and $TaCl_5$, as illustrated in Fig. 1a. The ionic conductivity of the cold-pressed pellets was assessed using the AC impedance method with Ti|SE|Ti ion-blocking symmetric cells. The corresponding Arrhenius plots of the ionic conductivities are presented in Fig. 1b, and the Nyquist plots are shown in Figure S1. The Arrhenius plots of ionic conductivities, comparing various K^+ SEs, can be found in Figure S2. BM-$KTaCl_6$ demonstrated a K^+ conductivity of 1.0×10^{-5} S cm^{-1} at 30 °C with an activation energy of 0.47 eV. Its electronic conductivity, determined through chronoamperometry tests, was observed to be sufficiently low at 8.3×10^{-10} S cm^{-1} (Figure S3). Conversely, HT-$KTaCl_6$ exhibited a much lower K^+ conductivity of 1.2×10^{-8} S cm^{-1} at 30 °C, with a considerably higher activation energy of 0.66 eV. The mechanisms underlying these distinct differences are discussed later.

The powder XRD patterns of BM- and HT-$KTaCl_6$ are shown in Fig. 1c. Despite the aim of achieving a $KTaCl_6$ composition from an equimolar mixture of KCl and $TaCl_5$, the XRD pattern of BM-$KTaCl_6$ corresponds to a cubic K_2MCl_6 phase (M = Ta (mp-31363), Sn (mp-23499)) with tetravalent M [42-44]. This result suggests that BM-$KTaCl_6$ may share a cubic K_2TaCl_6 structure but with a different stoichiometry. To ascertain the stoichiometry, a control sample was prepared by ball-milling KCl and $TaCl_5$ in a molar ratio of 2:1. The resultant XRD pattern displayed distinct impurity peaks of KCl (mp-23289) along with

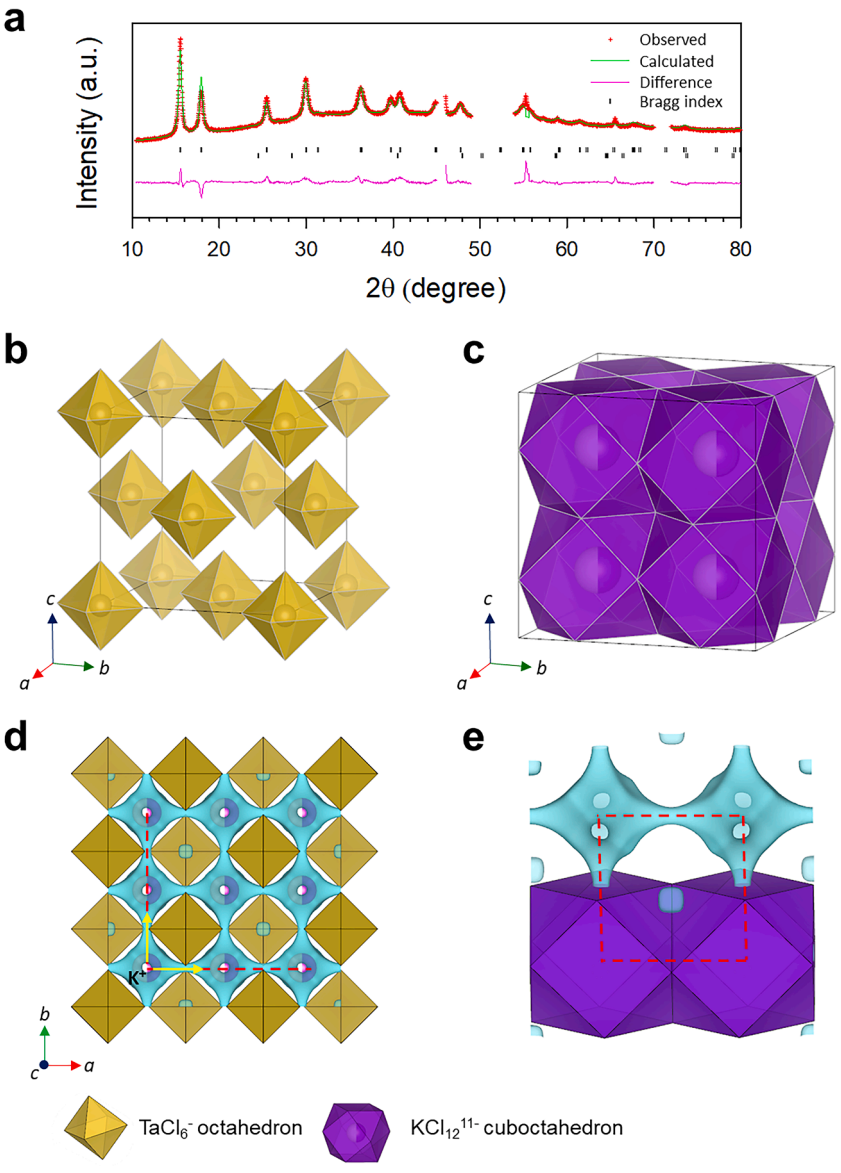

Fig. 2. Structural characterization of BM-$KTaCl_6$. a) XRD Rietveld refinement profiles for BM-$KTaCl_6$. The excluded ranges for the fitting were due to the presence of the Be window signals. The lower Bragg index corresponds to the peak of KCl, albeit in very small quantities. Crystal structure of BM-$KTaCl_6$ with the unit cell outlined, representing b) isolated $TaCl_6^-$ octahedra and c) face-sharing KCl_{12}^{11-} cuboctahedra. d, e) BVEL calculation results of BM-$KTaCl_6$. 3D K^+ migration pathways through the face-shared KCl_{12}^{11-} cuboctahedra are presented.

a cubic K_2TaCl_6 phase (mp-31363, Figure S4), confirming the stoichiometry of BM-$KTaCl_6$ as $KTaCl_6$ with pentavalent Ta. The oxidation state of Ta was further verified through X-ray photoelectron spectroscopy (XPS) measurements (Figure S5), where Ta 4f XPS peaks at 27.2 eV and 29.1 eV confirmed the presence of Ta in the 5+ oxidation state. Thus, it was conclusively determined that BM-$KTaCl_6$ has a $KTaCl_6$ stoichiometry and is isostructural with the cubic K_2TaCl_6 phase. In contrast to BM-$KTaCl_6$, which adopted a cubic structure, HT-$KTaCl_6$ exhibited a monoclinic structure (mp-1211251), as indicated in Fig. 1c. Details of the phases previously reported for $KTaCl_6$ are provided in the Supplementary Note [45].

XRD Rietveld refinement was performed to further elucidate the structures of BM- and HT-$KTaCl_6$. The refinement profiles for BM- and HT-$KTaCl_6$ are depicted in Figs. 2a and S6, respectively, and a comprehensive summary of the results is presented in Tables S2 and S3. BM-$KTaCl_6$ was found to have a cubic crystal structure with a lattice parameter of $a = 9.89367$ Å, and belongs to the $Fm\bar{3}m$ space group (space group no. 225). The detailed structure is visualized in Figs. 2b and c. Specifically, Ta^{5+} occupies the octahedral sites, forming isolated $TaCl_6^-$ octahedra (Fig. 2b). Owing to the substantial ionic size of K^+ (1.38 Å), it forms polyhedra with a high coordination number, specifically face-sharing KCl_{12}^{11-} cuboctahedra, which assemble into square-shaped K^+ channels with a bottleneck area of 11.5 $Å^2$ (Figs. 2d and e). Conversely, HT-$KTaCl_6$ was characterized by a monoclinic crystal structure with a $C2/c$ space group (space group no. 15). As depicted in Figure S7, the structure shares the features of isolated $TaCl_6^-$ octahedra with the cubic phase of BM-$KTaCl_6$. However, K^+ formed polyhedra of different shapes, i.e., a slightly distorted anti-cuboctahedra resembling a triangular orthobicupola [43,46]. Furthermore, their arrangement differed significantly from that of BM-$KTaCl_6$. Specifically, the KCl_{12}^{11-} anti-cuboctahedra are arranged in edge- or corner-sharing configurations, leading to the formation of a triangle-shaped K^+ channel with a bottleneck area of 5.4 $Å^2$ (Figure S7c). This area is significantly smaller than that of the BM-$KTaCl_6$ channels (11.5 $Å^2$).

Moreover, using structural parameters derived from the XRD Rietveld refinement (Figs. 2a and S6), BVEL analysis was conducted to visualize potential K^+ migration pathways in BM- and HT-$KTaCl_6$, as illustrated in Figs. 2d and S7, respectively. This analysis revealed interconnected K^+ pathways extending to all adjacent K sites, thereby establishing a comprehensive 3D network for K^+ migration. The isotropic nature of the cubic structure facilitates the formation of homogeneous 3D K^+ pathways in all directions (Figure S8). Various unit cell arrangements of cubic $KTaCl_6$ (BM-$KTaCl_6$) are shown in Figure S9. Conversely, the BVEL map for HT-$KTaCl_6$ reveals three inter-sites for K^+ migration and disconnected anisotropic K^+ migration pathways along the *a*, *b*, and *c* axes, as shown in Figures S7 and S10. In 1D migration, the pathway involves I1-I2-I1, whereas in 3D migration, it involves I1-I3, which has poor connectivity. In conclusion, the markedly different configurations of the K^+ migration pathways in terms of connectivity account for the ionic conductivity of BM-$KTaCl_6$, which is three orders of magnitude higher than that of HT-$KTaCl_6$.

First-principles calculations based on DFT were performed to assess

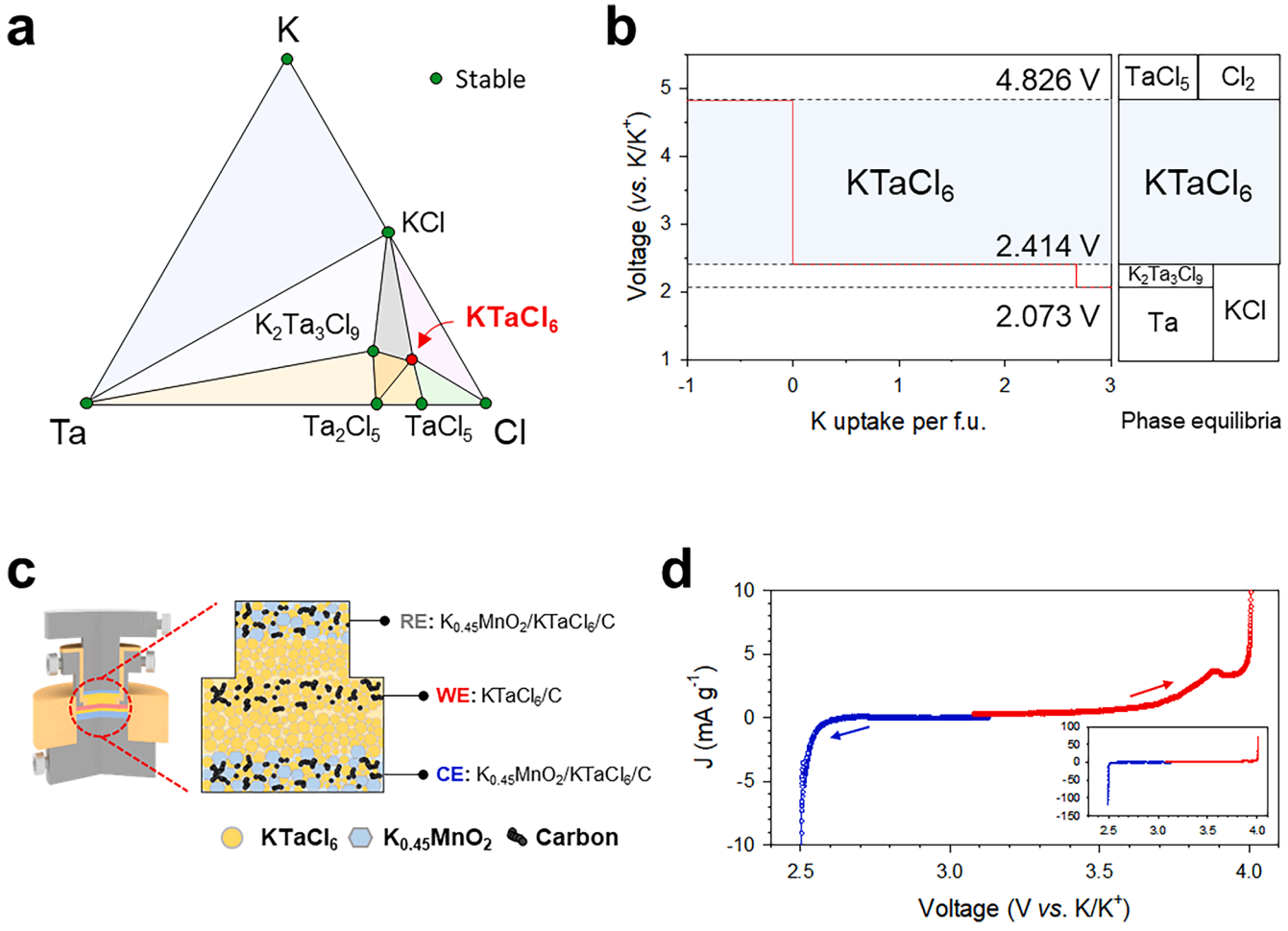

Fig. 3. Electrochemical stability of BM-$KTaCl_6$. a) Ternary phase diagram of K-Ta-Cl in the Materials Project Database. b) Intrinsic electrochemical stability window and phase equilibria of $KTaCl_6$ at different K/K^+ potentials based on first-principles calculations. c) Schematic of all-solid-state three-electrode cells using a $KTaCl_6$-C working electrode with $K_{0.45}MnO_2$-$KTaCl_6$-C as the reference and counter electrodes for CV measurements. d) CV results of BM-$KTaCl_6$ at 0.1 mV s^{-1} and 60 °C.

the intrinsic electrochemical stability of BM-$KTaCl_6$. This computational analysis was conducted within the stable phase diagram available in the Materials Project database; [47] the ternary phase diagrams for K-Ta-Cl are presented in Fig. 3a. The calculated electrochemical stability window and phase equilibria are shown in Fig. 3b. BM-$KTaCl_6$ exhibited a wide electrochemical stability range from 2.414 to 4.826 V (vs. K/K^+). At the anodic limit, the expected decomposition products include $K_2Ta_3Cl_9$ and KCl, whereas at the cathodic limit, $TaCl_5$ and Cl_2 are expected to form.

The electrochemical stability of BM-$KTaCl_6$ was experimentally evaluated via cyclic voltammetry (CV) using three-electrode cells with SE-C mixture electrodes in a weight ratio of 70:30. These measurements were conducted in the voltage range of 1.1–5.1 V (vs. K/K^+) in three-electrode cells at 60 °C, with the cell configuration depicted in Fig. 3c. Because of the instability of BM-$KTaCl_6$ when in contact with K metal, $K_{0.45}MnO_2$, which exhibited an initial potential of ≈3.1 V (vs. K/K^+), was chosen for both the counter and reference electrodes [48]. The initial voltage of $K_{0.45}MnO_2$ was determined using a coin cell configured as $K_{0.45}MnO_2$||K with a liquid electrolyte (1.5 M potassium bis(fluorosulfonyl)imide (KFSI) in a mixture of ethylene carbonate (EC) and diethylene carbonate (DEC) at a volume ratio of 1:1) at 30 °C (Figure S11). The cathodic and anodic stabilities were assessed using separate scans in the negative and positive directions, respectively, as shown in the CV results in Fig. 3d. The oxidation onset potential of BM-$KTaCl_6$ was observed to be ≈3.7 V (vs. K/K^+). Notably, this value surpasses that of sulfide K^+ SE $K_{2.92}Sb_{0.92}W_{0.08}S_4$, which is capable of operating cathodes in cells up to 3.0 V (vs. K/K^+) [13]. However, further positive scanning resulted in the severe oxidation at ≈4.0 V (vs. K/K^+). The voltage scan had to be terminated prematurely as the equipment's limitations were surpassed, resulting in an excessively high current, indicative of severe side reactions. In the negative scan, BM-$KTaCl_6$ exhibited poor reductive stability with the severe onset reduction potential at ≈2.5 V (vs. K/K^+).

The experimentally determined electrochemical stability window (2.7 ~ 3.7 V (vs. K/K^+)) is narrower than the estimates obtained from DFT calculations (2.414 ~ 4.826 V). This deviation can be attributed to the limited material space for K-Ta-Cl in the stable phase diagram provided by the Materials Project database (Fig. 3a) [47]. The calculated electrochemical window can be refined as more stable materials are identified.

Given the observed limitation in the reductive stability of $KTaCl_6$, we attempted to apply a polymer electrolyte, polyethylene oxide (PEO)-potassium bis(fluorosulfonyl)imide (KFSI) (PEO-KFSI), as an interlayer between BM-$KTaCl_6$ and K metal anode. Although the prepared PEO-KFSI films exhibited an acceptable K^+ conductivity of 6×10^{-4} S cm^{-1} at 60 °C, consistent with a previous report [49], they showed unstable interfacial stability with BM-$KTaCl_6$, inhibiting the construction of high-voltage all-solid-state K batteries (Figure S12). As an alternative, we employed $K_{0.45}MnO_2$ as both the cathode and anode, assembling $K_{0.45}MnO_2$|BM-$KTaCl_6$|$K_{0.45}MnO_2$ symmetric full cells. The corresponding results at 100 °C are presented in Figure S13. The $K_{0.45}MnO_2$|BM-$KTaCl_6$|$K_{0.45}MnO_2$ cells exhibited sloping voltage profiles similar to the simulated profiles (Figure S13a), obtained from liquid electrolyte cells (Figure S11). Despite their low capacities, demonstrating its reversible operation is noteworthy. Future development of interlayers compatible with both K metal and $KTaCl_6$ could enable the demonstration of all-solid-state K metal batteries. Additionally, the application of a reductively stable SE as an anolyte, such as sulfide SEs, could be an alternative direction [20,21,50], which will be the subject of our future research.

3. Conclusion

In summary, a new K^+ halide SE $KTaCl_6$ demonstrating an impressive K^+ conductivity of 1.0×10^{-5} S cm^{-1} at 30 °C was prepared via a mechanochemical method. Structural analyses through XRD Rietveld refinement revealed a cubic structure of BM-$KTaCl_6$, which is isostructural with the β phase of K_2TaCl_6. This cubic-structured BM-$KTaCl_6$ is characterized by KCl_{12}^{11-} cuboctahedra as its building units, which allow face-sharing connections and the formation of an extensive 3D network for K^+ migration, as revealed through BVEL analysis. In contrast, HT-$KTaCl_6$, which adopts a monoclinic structure, involves edge- and corner-sharing of KCl_{12}^{11-} anti-cuboctahedra, leading to disconnected K^+ migration pathways, and thus a substantially lower ionic conductivity of 1.2×10^{-8} S cm^{-1}. The electrochemical stability window of BM-$KTaCl_6$ was experimentally determined to be approximately 2.7 to 3.7 V (vs. K/K^+), through CV measurements utilizing all-solid-state three-electrode cells with $K_{0.45}MnO_2$ as both the counter and reference electrodes. This observation was further compared by DFT calculations. The notable voltage stability of $KTaCl_6$ highlights its potential as a promising catholyte for all-solid-state K batteries. This study opens avenues for the further enhancement of the K^+ conductivity of $KTaCl_6$ through substitution strategies.

4. Experimental section

4.1. Material preparation

For the preparation of BM-$KTaCl_6$, a stoichiometric mixture of KCl (99.0 %–100.5 %, Alfa Aesar) and $TaCl_5$ (99.99 %, Sigma Aldrich) was mechanically milled at 600 rpm in an Ar environment for 40 h in a 50 mL ZrO_2 vial with 15 ZrO_2 balls (ϕ = 10 mm) using a Pulverisette 7 PL (Fritsch GmbH). To prepare HT-$KTaCl_6$, a stoichiometric mixture of KCl and $TaCl_5$ was sealed in a quartz ampoule under vacuum, followed by heat treatment at 500 °C for 12 h at a heating rate of 5 °C min^{-1}. $K_{0.45}MnO_2$ was prepared using a conventional solid-state method. Stoichiometric amounts of K_2CO_3 (99 %, Alfa Aesar) and Mn_2O_3 (99.9 %, Sigma–Aldrich) were mechanically milled at 300 rpm for 4 h in an Ar environment in a 50 mL ZrO_2 vial with 15 ZrO_2 balls (ϕ = 10 mm) using a Pulverisette 7 PL (Fritsch GmbH). The resulting mixture was then heat-treated at 800 °C for 12 h in air.

4.2. Material characterization

Powder XRD patterns were obtained with a Rigaku MiniFlex600 diffractometer with Cu K_α radiation (λ = 1.5406 Å). At 40 kV and 15 mA, the XRD cells containing hermetically sealed SE samples with a Be window were placed on the X-ray diffractometer. The Rietveld refinement approach was used to obtain quantitative structural information using the FullProf Suite software. XPS measurements were conducted with a monochromatic Al K_α source (1486.6 eV) at 12 kV and 6 mA using KAlpha+ (Thermo Fisher Scientific). The samples were placed on a sample holder in an Ar-filled glove box and transported to the XPS equipment without exposure to air. SoftBV was used to perform BVEL calculations.

4.3. Electrochemical characterization

The AC impedance method was utilized to determine the K^+ conductivity using Ti|SE|Ti symmetric cells (ϕ = 6 mm). The cold-pressed pellets were prepared at 370 MPa. The EIS data were obtained using a VMP3 (BioLogic) instrument with an amplitude of 100 mV and a frequency range of 10 mHz to 7 MHz. For the CV measurements, the $K_{0.45}MnO_2$ counter and reference electrodes were used in the three-electrode cells. The counter and reference electrodes were prepared from a mixture of BM-$KTaCl_6$, $K_{0.45}MnO_2$, and Super C65 powder in a weight ratio of 50:50:5. The composite working electrodes were prepared from a mixture of BM-$KTaCl_6$ and Super C65 powders in a weight ratio of 70:30. All-solid-state three-electrode cells with a diameter of 13 mm, comprising Ti rods as the current collectors and a polyarylethetherketone (PEEK) mold, were assembled via the procedure described in a previous report [51]. First, SE layers were formed by

pelletizing 200 mg of $KTaCl_6$ powder at 100 MPa. The as-prepared working electrode was then spread on one side of the SE layer, whereas the counter electrode was placed on the other side, and the entire assembly was then pressed at 370 MPa. $KTaCl_6$ (120 mg) was placed on top of the working electrode. Finally, the reference electrode was placed on top of the $KTaCl_6$ layer and pressed at 70 MPa. The CV cells were tested under an external pressure of ≈70 MPa at 60 °C. The scan rate was 0.1 mV s^{-1}. To prepare the electrodes used for the coin cells, slurries were prepared from a mixture of N-methyl-2-pyrrolidinone (NMP) with $K_{0.45}MnO_2$, Super C65 powder, and poly(vinylidene fluoride) (PVDF) in a weight ratio of 80:10:10. These slurries were cast onto a piece of Al foil to form the electrodes. The mass loading of $K_{0.45}MnO_2$ on the electrodes was 8.2 mg cm^{-2}. K metal (Alfa Aesar) was used as the counter electrode. A glass-fiber sheet (GF/B, Whatman, USA) was used as the separator. A 1.5 M solution of KFSI dissolved in a mixture of EC/DEC (1:1 vol. ratio; PANAX ETEC) was used as the liquid electrolyte. The 2032-type coin cells were assembled in an Ar-filled glove box. For $K_{0.45}MnO_2|$BM-$KTaCl_6|K_{0.45}MnO_2$ cells, the counter and working electrodes were prepared from a mixture of BM-$KTaCl_6$, $K_{0.45}MnO_2$, and Super C65 powder in a weight ratio of 50:50:5. BM-$KTaCl_6$ powder (200 mg) was pelletized at 100 MPa to form SE layers. Then, the working and counter electrodes were placed on each side of the SE layers. Finally, the assemblies were pressed at 370 MPa. The mass loading of the cathode composite was 5.7 mg cm^{-2}. The all-solid-state cells were tested under an external pressure of ~70 MPa at 100 °C.

4.4. DFT calculations

DFT calculations were performed to evaluate the electrochemical stability. The Vienna Ab initio Simulation Package (VASP) [52] program with the projector-augmented wave (PAW) method was used for the DFT calculations. The $KTaCl_6$ structure was calculated using the generalized gradient approximation (GGA) with the Perdew–Burke–Ernzerhof functional [53] for exchange correlation. We prepared the structure of $KTaCl_6$ from the Rietveld refinement results and calculated the symmetric distinct K and vacancy ordering at the K sites. By enumeration method, the most stable configuration was used to calculate the electrochemical stability. The crystal structures of all the relevant phases (K, Ta, Cl_2, KCl, $K_2Ta_3Cl_9$, Ta_2Cl_5, and $TaCl_5$) were obtained from the Materials Project database [47], and their grand potential phase diagrams were used to evaluate the electrochemical stability windows using the Pymatgen package [54]. The decomposition reaction energy was defined as follows:

$$\Delta E_D = E_{eq}(Phase\ equlibria,\ \mu_K) - E_{SE}(phase)\Delta n_k \mu_k$$

where μ_K is the chemical potential of potassium, and Δn_k is the number difference of the element K from the original composition.

CRediT authorship contribution statement

Changhoon Kim: Writing – original draft, Methodology, Investigation, Data curation, Conceptualization. **Juhyoun Park:** Methodology, Investigation, Conceptualization. **Hiram Kwak:** Methodology, Conceptualization. **Jae-Seung Kim:** Investigation, Formal analysis. **Seunggoo Jun:** Methodology, Formal analysis. **Dong-Hwa Seo:** Supervision. **Yoon Seok Jung:** Writing – review & editing, Supervision, Conceptualization.

Declaration of competing interest

The authors declare that they have no known competing financial interests or personal relationships that could have appeared to influence the work reported in this paper.

Acknowledgements

This research was supported by the National Research Foundation of Korea (NRF) grant funded by the Korea government (MSIT) (RS-2024-00343349, RS-2023-00261543, and 2023R1A2C2008242). The computational work was supported by the Supercomputing Center/Korea Institute of Science and Technology Information with supercomputing resources including technical support (KSC-2023-CRE-0513 to D.-H.S.).

Supplementary materials

Supplementary material associated with this article can be found, in the online version, at doi:10.1016/j.ensm.2024.103618.

References

[1] K. Kubota, M. Dahbi, T. Hosaka, S. Kumakura, S. Komaba, Towards K-ion and Na-ion batteries as "beyond Li-ion, Chem. Rec. 18 (2018) 459–479, https://doi.org/10.1002/tcr.201700057.
[2] Y. Marcus, Thermodynamic functions of transfer of single ions from water to nonaqueous and mixed solvents: part 3-Standard potentials of selected electrodes, Pure Appl. Chem. 57 (1985) 1129–1132, https://doi.org/10.1351/pac198557081129.
[3] R. Rajagopalan, Y. Tang, X. Ji, C. Jia, H. Wang, Advancements and challenges in potassium ion batteries: a comprehensive review, Adv. Funct. Mater. 30 (2020) 1909486, https://doi.org/10.1002/adfm.201909486.
[4] J.C. Pramudita, D. Sehrawat, D. Goonetilleke, N. Sharma, An initial review of the status of electrode materials for potassium-ion batteries, Adv. Energy Mater. 7 (2017) 1602911, https://doi.org/10.1002/aenm.201602911.
[5] C. Arbizzani, G. Gabrielli, M. Mastragostino, Thermal stability and flammability of electrolytes for lithium-ion batteries, J. Power Sources 196 (2011) 4801–4805, https://doi.org/10.1016/j.jpowsour.2011.01.068.
[6] J. Wang, Y. Yamada, K. Sodeyama, E. Watanabe, K. Takada, Y. Tateyama, A. Yamada, Fire-extinguishing organic electrolytes for safe batteries, Nat. Energy 3 (2018) 22–29, https://doi.org/10.1038/s41560-017-0033-8.
[7] K. Liu, Y. Liu, D. Lin, A. Pei, Y. Cui, Materials for lithium-ion battery safety, Sci. Adv. 4 (2018) eaas9820, https://doi.org/10.1126/sciadv.aas9820.
[8] J.W. Choi, D. Aurbach, Promise and reality of post-lithium-ion batteries with high energy densities, Nat. Rev. Mater. 1 (2016) 1–16, https://doi.org/10.1038/natrevmats.2016.13.
[9] H. Huo, J. Janek, Solid-state batteries: from 'all-solid'to 'almost-solid, Natl. Sci. Rev. 10 (2023) nwad098, https://doi.org/10.1093/nsr/nwad098.
[10] H. Yuan, H. Li, T. Zhang, G. Li, T. He, F. Du, S. Feng, AK 2 Fe 4 O 7 superionic conductor for all-solid-state potassium metal batteries, J. Mater. Chem. 6 (2018) 8413–8418, https://doi.org/10.1039/C8TA01418C. A.
[11] A.C. Baclig, G. McConohy, A. Poletayev, A. Michelson, N. Kong, J.-H. Lee, W.C. Chueh, J. Rugolo, High-voltage, room-temperature liquid metal flow battery enabled by Na-K| K-β″-alumina stability, Joule 2 (2018) 1287–1296. https://doi.org/10.1016/j.joule.2018.04.008.
[12] J. Shao, J. Zheng, L. Qin, S. Zhang, Y. Ren, Y. Wu, K3SbS4 as a potassium superionic conductor with low activation energy for K–S batteries, Angew. Chem. 134 (2022) e202200606, https://doi.org/10.1002/ange.202200606.
[13] J. Shao, H. Ao, L. Qin, J. Elgin, C.E. Moore, Y. Khalifa, S. Zhang, Y. Wu, Design and synthesis of cubic K3− 2xBaxSbSe4 solid electrolytes for K–O2 batteries, Adv Mater 35 (2023) 2306809, https://doi.org/10.1002/adma.202306809.
[14] A. Sakuda, A. Hayashi, M. Tatsumisago, Sulfide solid electrolyte with favorable mechanical property for all-solid-state lithium battery, Sci. Rep. 3 (2013) 2261, https://doi.org/10.1038/srep02261.
[15] J.E. Huheey, E.A. Keiter, R.L. Keiter, O.K. Medhi, Inorganic Chemistry: Principles of Structure and Reactivity, Pearson Education India, 2006.
[16] K.H. Park, D.Y. Oh, Y.E. Choi, Y.J. Nam, L. Han, J.Y. Kim, H. Xin, F. Lin, S.M. Oh, Y. S. Jung, Solution-processable glass LiI-Li4SnS4 superionic conductors for all-solid-state Li-ion batteries, Adv. Mater. 28 (2016) 1874–1883, https://doi.org/10.1002/adma.201505008.
[17] L. Zhou, K.-H. Park, X. Sun, F. Lalère, T. Adermann, P. Hartmann, L.F. Nazar, Solvent-engineered design of argyrodite Li6PS5X (X= Cl, Br, I) solid electrolytes with high ionic conductivity, ACS Energy Lett. 4 (2018) 265–270, https://doi.org/10.1021/acsenergylett.8b01997.
[18] C.K. Moon, H.-J. Lee, K.H. Park, H. Kwak, J.W. Heo, K. Choi, H. Yang, M.-S. Kim, S.-T. Hong, J.H. Lee, Y.S. Jung, Vacancy-driven Na+ superionic conduction in new Ca-doped Na3PS4 for all-solid-state Na-ion batteries, ACS Energy Lett. 3 (2018) 2504–2512, https://doi.org/10.1021/acsenergylett.8b01479.
[19] T. Asano, A. Sakai, S. Ouchi, M. Sakaida, A. Miyazaki, S. Hasegawa, Solid halide electrolytes with high lithium-ion conductivity for application in 4 V class bulk-type all-solid-state batteries, Adv Mater 30 (2018) 1803075, https://doi.org/10.1002/adma.201803075.
[20] H. Kwak, S. Wang, J. Park, Y. Liu, K.T. Kim, Y. Choi, Y. Mo, Y.S. Jung, Emerging halide superionic conductors for all-solid-state batteries: design, synthesis, and practical applications, ACS Energy Lett. 7 (2022) 1776–1805, https://doi.org/10.1021/acsenergylett.2c00438.

[21] Y. Han, S.H. Jung, H. Kwak, S. Jun, H.H. Kwak, J.H. Lee, S.T. Hong, Y.S. Jung, Single-or poly-crystalline Ni-rich layered cathode, sulfide or halide solid electrolyte: which will be the winners for all-solid-state batteries? Adv. Energy Mater. 11 (2021) 2100126 https://doi.org/10.1002/aenm.202100126.
[22] K. Kim, D. Park, H.-G. Jung, K.Y. Chung, J.H. Shim, B.C. Wood, S. Yu, Material design strategy for halide solid electrolytes Li3MX6 (X= Cl, Br, and I) for all-solid-state high-voltage Li-ion batteries, Chem. Mater. 33 (2021) 3669–3677, https://doi.org/10.1021/acs.chemmater.1c00555.
[23] X. Li, J. Liang, J. Luo, M.N. Banis, C. Wang, W. Li, S. Deng, C. Yu, F. Zhao, Y. Hu, T.-K. Sham, L. Zhang, S. Zhao, S. Lu, H. Huang, R. Li, K.R. Adair, X. Sun, Air-stable Li 3 InCl 6 electrolyte with high voltage compatibility for all-solid-state batteries, Energy Environ. Sci. 12 (2019) 2665–2671, https://doi.org/10.1039/C9EE02311A.
[24] J. Liang, X. Li, S. Wang, K.R. Adair, W. Li, Y. Zhao, C. Wang, Y. Hu, L. Zhang, S. Zhao, S. Lu, H. Huang, R. Li, Y. Mo, X. Sun, Site-occupation-tuned superionic Li x ScCl3+ x halide solid electrolytes for all-solid-state batteries, J. Am. Chem. Soc 142 (2020) 7012–7022, https://doi.org/10.1021/jacs.0c00134.
[25] H. Kwak, D. Han, J. Lyoo, J. Park, S.H. Jung, Y. Han, G. Kwon, H. Kim, S.T. Hong, K.W. Nam, Y.S. Jung, New cost-effective halide solid electrolytes for all-solid-state batteries: mechanochemically prepared Fe3+-substituted Li2ZrCl6, Adv. Energy Mater. 11 (2021) 2003190, https://doi.org/10.1002/aenm.202003190.
[26] K.-H. Park, K. Kaup, A. Assoud, Q. Zhang, X. Wu, L.F. Nazar, High-voltage superionic halide solid electrolytes for all-solid-state Li-ion batteries, ACS Energy Lett. 5 (2020) 533–539, https://doi.org/10.1021/acsenergylett.9b02599.
[27] J. Liang, E. van der Maas, J. Luo, X. Li, N. Chen, K.R. Adair, W. Li, J. Li, Y. Hu, J. Liu, L. Zhang, S. Zhao, S. Lu, J. Wang, H. Huang, W. Zhao, S. Parnell, R.I. Smith, S. Ganapathy, M. Wagemaker, X. Sun, A series of ternary metal chloride superionic conductors for high-performance all-solid-state lithium batteries, Adv. Energy Mater. 12 (2022) 2103921, https://doi.org/10.1002/aenm.202103921.
[28] H. Kwak, J. Lyoo, J. Park, Y. Han, R. Asakura, A. Remhof, C. Battaglia, H. Kim, S.-T. Hong, Y.S. Jung, Na2ZrCl6 enabling highly stable 3 V all-solid-state Na-ion batteries, Energy Storage Mater 37 (2021) 47–54, https://doi.org/10.1016/j.ensm.2021.01.026.
[29] R. Schlem, A. Banik, M. Eckardt, M. Zobel, W.G. Zeier, Na3–x Er1–x Zr x Cl6—A Halide-Based Fast Sodium-Ion Conductor with Vacancy-Driven Ionic Transport, ACS Appl. Energy Mater. 3 (2020) 10164–10173, https://doi.org/10.1021/acsaem.0c01870.
[30] E.A. Wu, S. Banerjee, H. Tang, P.M. Richardson, J.-M. Doux, J. Qi, Z. Zhu, A. Grenier, Y. Li, E. Zhao, G. Deysher, E. Sebti, H. Nguyen, R. Stephens, G. Verbist, K.W. Chapman, R.J. Clément, A. Banerjee, Y.S. Meng, S.P. Ong, A stable cathode-solid electrolyte composite for high-voltage, long-cycle-life solid-state sodium-ion batteries, Nat. Commun 12 (2021) 1256, https://doi.org/10.1038/s41467-021-21488-7.
[31] J. Park, D. Han, J.P. Son, H. Kwak, W. Ko, C. Park, C. Lee, H.-W. Lee, J. Kim, K.-W. Nam, Y.S. Jung, Extending the Electrochemical Window of Na+ Halide Nanocomposite Solid Electrolytes for 5 V-Class All-Solid-State Na-Ion Batteries, ACS Energy Letters 9 (2024) 2222–2230, https://doi.org/10.1021/acsenergylett.4c00490.
[32] Y. Ishiguro, K. Ueno, S. Nishimura, G. Iida, Y. Igarashib, TaCl5-glassified ultrafast lithium ion-conductive halide electrolytes for high-performance all-solid-state lithium batteries, Chem. Lett. 52 (2023) 237–241, https://doi.org/10.1246/cl.220540.
[33] Y. Tanaka, K. Ueno, K. Mizuno, K. Takeuchi, T. Asano, A. Sakai, New oxyhalide solid electrolytes with high lithium ionic conductivity>10 mS cm− 1 for all-solid-state batteries, Angew. Chem. 135 (2023) e202217581, https://doi.org/10.1002/ange.202217581.
[34] J. Park, J.P. Son, W. Ko, J.-S. Kim, Y. Choi, H. Kim, H. Kwak, D.-H. Seo, J. Kim, Y. S. Jung, NaAlCl4: new halide solid electrolyte for 3 V stable cost-effective all-solid-state Na-ion batteries, ACS Energy Lett. 7 (2022) 3293–3301, https://doi.org/10.1021/acsenergylett.2c01514.
[35] Y. Hu, J. Fu, J. Xu, J. Luo, F. Zhao, H. Su, Y. Liu, X. Lin, W. Li, J.T. Kim, X. Hao, X. Yao, Y. Sun, J. Ma, H. Ren, M. Yang, Y. Huang, X. Sun, Superionic amorphous NaTaCl6 halide electrolyte for highly reversible all-solid-state Na-ion batteries, Matter (2024), https://doi.org/10.1016/j.matt.2023.12.017.
[36] K. Motohashi, H. Tsukasaki, A. Sakuda, S. Mori, A. Hayashi, NaTaCl6: chloride as the end-member of sodium-ion conductors, ACS mater. lett. 6 (2024) 1178–1183, https://doi.org/10.1021/acsmaterialslett.3c01445.
[37] X. Lin, Y. Zhao, C. Wang, J. Luo, J. Fu, B. Xiao, Y. Gao, W. Li, S. Zhang, J. Xu, F. Yang, X. Hao, H. Duan, Y. Sun, J. Guo, Y. Huang, X. Sun, A Dual Anion Chemistry-Based Superionic Glass Enabling Long-Cycling All-Solid-State Sodium-Ion Batteries, Angew. Chem., Int. Ed. (2023) e202314181, https://doi.org/10.1002/ange.202314181.
[38] S. Wang, J. Fu, Y. Liu, R.S. Saravanan, J. Luo, S. Deng, T.-K. Sham, X. Sun, Y. Mo, Design principles for sodium superionic conductors, Nat. Commun. 14 (2023) 7615, https://doi.org/10.1038/s41467-023-43436-3.
[39] Y. Okada, A. Nasu, T. Kimura, H. Tsukasaki, S. Mori, H. Ben Yahia, K. Motohashi, A. Sakuda, A. Hayashi, Mechanochemical synthesis and characterization of K2+ x Zr1–x Y x Cl6: potassium-ion-conducting chloride, Chem. Mater. 35 (2023) 7422–7429, https://doi.org/10.1021/acs.chemmater.3c00185.
[40] X. Li, Y. Xu, C. Zhao, D. Wu, L. Wang, M. Zheng, X. Han, S. Zhang, J. Yue, B. Xiao, W. Xiao, L. Wang, T. Mei, M. Gu, J. Liang, X. Sun, The universal super cation-conductivity in multiple-cation mixed chloride solid-state electrolytes, Angew. Chem. Int. Ed. 62 (2023) e202306433, https://doi.org/10.1002/anie.202306433.
[41] J.D. Luo, Y. Zhang, X. Cheng, F. Li, H.Y. Tan, M.Y. Zhou, Z.W. Wang, X.D. Hao, Y. C. Yin, B. Jiang, H.-B. Yao, Halide superionic conductors with non-close-packed anion frameworks, Angewandte Chemie Int. Ed. 63 (2024) e202400424, https://doi.org/10.1002/anie.202400424.
[42] X. Yang, Y. Shi, K. Xie, S. Fang, Y. Zhang, Y. Deng, Cocrystallization enabled spatial self-confinement approach to synthesize crystalline porous metal oxide nanosheets for gas sensing, Angew. Chem. 134 (2022) e202207816, https://doi.org/10.1002/ange.202207816.
[43] E. Bikanina, A. Shevchenko, V. Serezhkin, The coordination polyhedra KCl n in the crystal structures, Russ. J. Coord. Chem. 31 (2005) 68–76, https://doi.org/10.1007/s11173-005-0013-6.
[44] L. Jongen, G. Meyer, Dipotassium hexachlorotantalate (IV), K2TaCl6, Acta. Crystallogr. B. Struct. Sci. Cryst. Eng. Mater. 60 (2004) i91–i92, https://doi.org/10.1107/S1600536804016198.
[45] F. Poulsen, N. Andersen, K. Clausen, D. Sadoway, L. Øgendal, Super ionic conduction in alkali metal hexachloro niobates and tantalates, Solid State Ion 28 (1988) 271–275, https://doi.org/10.1016/S0167-2738(88)80049-3.
[46] H. Shen, K. Kubo, S. Kume, L. Zhang, T. Mizuta, Novel chloride-centered Ag 18 clusters featuring a cuboctahedral Ag 12 skeleton, Dalton Trans. 46 (2017) 16199–16204, https://doi.org/10.1039/C7DT03195E.
[47] A. Jain, S.P. Ong, G. Hautier, W. Chen, W.D. Richards, S. Dacek, S. Cholia, D. Gunter, D. Skinner, G. Ceder, K.A. Persson, Commentary: the materials project: a materials genome approach to accelerating materials innovation, APL Mater. (2013) 1, https://doi.org/10.1063/1.4812323.
[48] Y. Huang, X. Zhang, H. Lin, Z. Wei, Y. Zeng, X. Ge, W. Zhang, X. Wang, X. Jin, Z. X. Shen, F. Du, Synergistically enhanced structural, thermal and interfacial stability of K0. 45MnO2 via tailoring the local structure for high-energy and high-power potassium-ion batteries, J. Chem. Eng. 453 (2023) 139571, https://doi.org/10.1016/j.cej.2022.139571.
[49] H. Fei, Y. Liu, Y. An, X. Xu, J. Zhang, B. Xi, S. Xiong, J. Feng, Safe all-solid-state potassium batteries with three dimentional, flexible and binder-free metal sulfide array electrode, J. Power Sources 433 (2019) 226697, https://doi.org/10.1016/j.jpowsour.2019.226697.
[50] H. Kwak, J.-S. Kim, D. Han, J.S. Kim, J. Park, G. Kwon, S.-M. Bak, U. Heo, C. Park, H.-W. Lee, K.W. Nam, D.-H. Seo, Y.S. Jung, Boosting the interfacial superionic conduction of halide solid electrolytes for all-solid-state batteries, Nat. Commun 14 (2023) 2459, https://doi.org/10.1038/s41467-023-38037-z.
[51] Y.J. Nam, K.H. Park, D.Y. Oh, W.H. An, Y.S. Jung, Diagnosis of failure modes for all-solid-state Li-ion batteries enabled by three-electrode cells, J. Mater. Chem. 6 (2018) 14867–14875, https://doi.org/10.1039/C8TA03450H. A.
[52] G. Kresse, J. Furthmüller, Efficient iterative schemes for ab initio total-energy calculations using a plane-wave basis set, Physical review 54 (1996) 11169, https://doi.org/10.1103/PhysRevB.54.11169. B.
[53] J.P. Perdew, K. Burke, M. Ernzerhof, Generalized gradient approximation made simple, Phys. Rev. Lett. 77 (1996) 3865, https://doi.org/10.1103/PhysRevLett.77.3865.
[54] S.P. Ong, L. Wang, B. Kang, G. Ceder, Li− Fe− P−, O2 phase diagram from first principles calculations, Chem. Mater. 20 (2008) 1798–1807, https://doi.org/10.1021/cm702327g.